

A full-dimension intra- and inter-molecular *ab initio* potential energy surface and predicted infrared spectra for H₂O-He

Dan Hou, Yong-Tao Ma, Xiao-Long Zhang, Hui Li *

Institute of Theoretical Chemistry, Jilin University, 2519 Jiefang Road, Changchun 130023, PR China

ARTICLE INFO

Article history:

Received 16 May 2016

In revised form 12 July 2016

Accepted 20 July 2016

Available online 22 July 2016

Keywords:

H₂O-He

Potential energy surface

Infrared spectrum

Normal modes

ABSTRACT

A full-dimension intra- and inter-molecular *ab initio* potential energy surface (PES) for H₂O-He, which explicitly incorporates dependence on the intra-molecular (Q_1 , Q_2 , Q_3) normal-mode coordinates of the H₂O monomer has been calculated in this work. In addition, three analytic vibrational-quantum-state-specific PESs are obtained by least-squares fitting vibrationally averaged interaction energies for the $(v_1, v_2, v_3) = (0, 0, 0)$, $(0, 0, 1)$ and $(0, 1, 0)$ states of H₂O to the three-dimensional Morse/long-range potential function. Each vibrationally averaged PES fitted to 578 points has root-mean-square (rms) deviation smaller than 0.1 cm^{-1} , and required only 53 parameters. With the 3D PESs of the H₂O-He dimer system, we employed the **combined radial discrete variable representation/angular finite basis representation method and Lanczos algorithm to calculate rovibrational energy levels**. The rovibrational spectra and their relative intensities for the H₂O-He complex have been predicted for the first time.

© 2016 Elsevier Inc. All rights reserved.

1. Introduction

Water is one of the most important interstellar molecules and has a prominent role in collision phenomena involving other particle in a variety of astrophysical and atmospheric environments. Among them, the H₂O-He collisional system is a typical non-local thermodynamic equilibrium (NLTE) model [1,2]. For the NLTE models, the knowledge of state-to-state rotational and rate coefficients is crucial, and prediction of the rotational and vibrational spectrum in a variety of astrophysical environment is also needed. In 1975, Kung and Center studied the vibrational relaxation of H₂O by He behind incident shock waves at temperatures between 1800 and 4100 K [3]. Since, helium is the second most abundant partner of H₂O in planetary atmospheres and the interstellar medium, the H₂O-He system has been the focus of state-to-state rotational and rate coefficient calculations and of numerous experimental and theoretical studies. However, the available experimental data are difficult to interpret, as are the results of astrophysical microwave spectroscopic measurements concerning the constituents of the planetary atmospheres and interstellar gas [4,5]. Although Ar-H₂O [6–16], Ar-D₂O [17], Xe-H₂O [18], Kr-H₂O [19] and Ne-D₂O [20] complexes were studied by microwave or high resolution infrared spectroscopy, even the spectra of v_1 and v_3

ro-vibrational bands [21] and the high-resolution infrared spectra [22] of water molecules in He droplets have been obtained. H₂O-He is a good example of an asymmetric top that “freely rotates” in the complex. However, as far as we know, no spectra have yet been reported for the lighter H₂O-He dimer. The infrared spectra for He-CO [23,24] and He-C₂D₂ [25] have been reported by McKellar and his co-workers, that illuminate the spectrum for H₂O-He, which has nearly equal intermolecular interaction force as those of He-CO and He-C₂D₂, is likely to be observed. Recently, theory untangles the high-resolution infrared spectrum of the ortho-H₂-CO [26,27] van der Waals complex based on the high-accuracy quantum mechanical computations. The rather complex spectrum has been unexplained for more than a decade. Thus, first and foremost, an accurate potential energy surfaces (PES) is required to allow for reliable theoretical simulations for the H₂O-He system.

The first electron gas model potential was developed by Green in 1980 [28], and he suggested that the rate constants for water molecules in collisions with He could be derived from *ab initio* calculations. Green and his co-workers [29–34] then investigated the excitation of H₂O with He in a series of increasingly sophisticated calculations on improved potentials. Palma et al. [29] reported two *ab initio* surfaces obtained using Møller-Plesset (MP4) method and the interacting correlated fragments (ICF1) theory. The ICF1 surface appeared to be marginally better than the MP4 surface from comparison with the limited experimental data. Green [32] improved the potential energy surfaces of Palma in 1991, and the

* Corresponding author.

E-mail address: Prof_huili@jlu.edu.cn (H. Li).

broadening cross section computed from the new surfaces differed by 10–30% from the results obtained using the old surfaces. Maluendes et al. [33] continued to improve the MP4 and ICF1 potentials by calculating the interaction at additional orientations and including diffuse functions in the molecular orbital expansion basis set. Then, in 1993 Green et al. [34] calculated the theoretical rotationally inelastic rate constants among the lowest 45 para and 45 ortho rotational levels of H₂O in collisions with He atoms for temperatures between 20 and 2000 K, using the improved interaction potential of Ref. [33]. This demonstrated that having a more accurate potential energy surface is crucial for improving the quality of predicted the scattering dynamics results for comparison with experimental data for the H₂O-He collision pair.

There were also other *ab initio* PESs for the H₂O-He system. In 1993, Kukawska-Marnawska et al. [35] obtained a potential with a well depth of 29.9 cm⁻¹, which is deeper than those of the previous PESs. Tao and his co-workers [36] calculated the intermolecular potential surface for the He-H₂O using complete fourth-order Møller-Plesset perturbation theory (MP4) with an efficient basis set containing bond functions. In 2002, Hodges et al. [37] presented a H₂O-He PES that was constructed from scaled perturbation theory (SAPT) calculations and calibrated using accurate supermolecule methods. This potential was used to calculate second virial coefficients at temperatures from 100 to 2000 K [37]. Meanwhile, Patkowski et al. [38] developed a new H₂O-He PES with SAPT using larger basis sets (159 functions of spd² symmetry) and more grid points (242 total) than had been used in the previous PES. Later, Calderoni et al. [39] calculated the PESs of H₂O-He based on Coupled-Cluster, Møller-Plesset, and valence bond (VB) methods. In this work, they determined the rovibrational structure of the complex under the assumption that H₂O molecule rotates freely, and predicted the H₂O-He complex to have a single bound vibrational state and three rotational excitations. Recently, Makarewicz [40] constructed a highly accurate analytical H₂O-He PES by calculating more than 430 single-point interaction energies at the CCSD(T) level, extrapolated to the complete basis set (CBS) limit. Most rotational cross sections and state-to-state rate coefficients of H₂O collisions with He [1,41,2,42,43] have been obtained from the PESs of Ref. [37], Ref. [38] or Ref. [39].

Involving the intramolecular vibrational coordinates in the potential energy surfaces and bound states calculations for van der Waals complexes is essential for fully predicting the vibrational spectra of the complexes [44]. However, to date there has been no inter-molecular PES for H₂O-He, which included the intramolecular vibrational modes of H₂O monomer. Recently, we determined a full six-dimensional (6D) potential energy surface for the H₂O-Ar [45] system that explicitly depends on the three intramolecular vibrational modes of H₂O. The predicted infrared transitions for *para*-H₂O-Ar and *ortho*-H₂O-Ar are in good agreement with the experimental results. In the present work, a new six-dimensional (6D) potential energy surface for H₂O-He is presented which incorporates three intramolecular vibrational modes of H₂O, and is expected to be just as accurate as that for H₂O-Ar. The intermolecular interaction of H₂O-He is computed at the CCSD(T)/aug-cc-pVQZ level with bond functions. After vibrational averaging over three intramolecular coordinates, the resulting PESs were fitted to three-dimensional Morse/long-range (MLR) functional forms. The MLR form explicitly incorporates the theoretically known inverse-power long range behavior and its anisotropy and dependence on the intramolecular stretch coordinates. Using these PESs, we first predicted the microwave and infrared spectra for *para*-H₂O-He and *ortho*-H₂O-He complexes, respectively.

This paper is arranged as follows. The *ab initio* calculations used for the generating potential energy surface, and the details for computing the eigenvalues are described in Section 2. Section 3

presents the predictions of the microwave and infrared spectra for H₂O-He by this surface. A discussion of the results, and overall conclusions are then given in Section 4.

2. Theoretical method

2.1. *Ab initio* calculations detail

The body-fixed Jacobi coordinates ($R, \theta, \phi, Q_1, Q_2, Q_3$) used in this work are shown in Fig. 1(a). (R, θ, ϕ) are the intermonomer coordinates that describe the relative positions of the H₂O and the He, with \vec{R} being a vector pointing from the center of mass of the H₂O to the He atom, θ the angle between \vec{R} and the C₂ axis of H₂O, ϕ the dihedral angle between the two planes defined by \vec{R} with C₂ and the H₂O molecule plane, while Q_1, Q_2 , and Q_3 are the intramonomer coordinates which describe the symmetric stretch, bending and asymmetric stretch modes, respectively, of the H₂O molecule.

On including the intramolecular vibrational coordinates Q_1, Q_2 and Q_3 of H₂O, the total potential energy for H₂O-He can be written as

$$V(R, \theta, \phi, Q_1, Q_2, Q_3) = V_{\text{H}_2\text{O}}(Q_1, Q_2, Q_3) + \Delta V(R, \theta, \phi, Q_1, Q_2, Q_3) \quad (1)$$

in which, $V_{\text{H}_2\text{O}}(Q_1, Q_2, Q_3)$ is the three-dimensional (3D) intramolecular potential energy surface, and $\Delta V(R, \theta, \phi, Q_1, Q_2, Q_3)$ is the 6D intermolecular interaction potential. The 3D intramolecular PES of $V_{\text{H}_2\text{O}}(Q_1, Q_2, Q_3)$ governing the Q_1, Q_2 and Q_3 vibration of the isolated H₂O monomer was determined by Polyansky et al. [46] from experimental spectroscopic data.

The intermolecular potential energies of H₂O-He were calculated at the CCSD(T) [47]/aug-cc-pVQZ [48] level, supplemented with an additional set of bond functions (3s3p2d1f1g) (where $\alpha = 0.9, 0.3, 0.1$, for 3s and 3p; $\alpha = 0.6, 0.2$, for 2d; $\alpha = 0.3$, for f and g) placed at the mid-point of the intermolecular axis R . [49,50] The supermolecule approach was used to produce the intermolecular potential energy $\Delta V(R, \theta, \phi, Q_1, Q_2, Q_3)$, which is defined as the difference between the energy of the H₂O-He complex and the sum of the energies of the H₂O and He monomers. The full counterpoise procedure was employed to correct for the basis set superposition error (BSSE). [51] All calculations were carried out using the MOLPRO package [52].

For the 6D PESs, a total of 72,250 symmetry-unique *ab initio* points were calculated. The calculations were performed on regular grids for all six degrees of freedom. For three intra-molecular normal modes (Q_1, Q_2, Q_3) of H₂O, 125 potential-optimized discrete variable representation (PODVR) [53,54] grid points

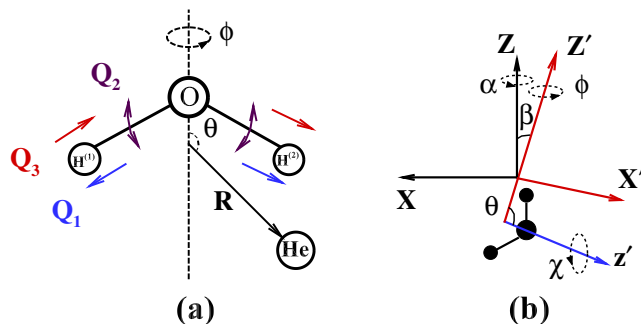


Fig. 1. (a) Jacobi coordinates used to generate our 6D $\Delta V(R, \theta, \phi, Q_1, Q_2, Q_3)$ for H₂O-He; and (b) frames used in present work to calculate the rovibrational energy levels of the *ortho*-H₂O-He and *para*-H₂O-He complexes.

corresponding to $Q_1 = -0.26213, -0.14910, -0.05257, 0.03906, 0.13512 \text{ \AA}$, $Q_2 = -0.30783, -0.15392, -0.01604, 0.12024, 0.26959 \text{ \AA}$ and $Q_3 = -0.18018, -0.08600, 0.0, 0.08600, 0.18018 \text{ \AA}$ were used at for a large number of geometries on a (R, θ, ϕ) grid, which are the same as those used for $\text{H}_2\text{O}-\text{Ar}$ complex [45], where the unit should be bohr. A relatively dense grid was used that included 13 values of R (\AA) = [2.2, 2.4, 2.6, 2.8, 3.0, 3.2, 3.4, 3.6, 3.8, 4.0, 4.2, 4.5, 5.0, 6.0, 8.0, 9.0, 10.0], 13 values of the polar angle θ ($^\circ$) evenly distributed from 0 to 180° at interval of 15° , and dihedral angles ϕ ranging from 0 to 90° at interval of 30° .

Our vibrationally averaged *ab initio* intermolecular potential energies for $\text{H}_2\text{O}-\text{Ar}$ were fitted to a three-dimensional MLR potential function using the same approach as Ref. [45]. The long-range \bar{C}_6 coefficients $\bar{C}_6 = \bar{C}_{6,\text{ind}} + \bar{C}_{6,\text{disp}}$, where $\bar{C}_{6,\text{disp}}$ and $\bar{C}_{6,\text{ind}}$ refer to dispersion and induction coefficients. The vibrational ground-state coefficient $\bar{C}_{6,\text{disp}}^{(0,0,0)}$ is obtained from the calculated data. [29] The fitting details were described in Ref. [45]. The resulting sets of potential parameters and a FORTRAN subroutine for generating these potentials may be obtained from the authors or from the journal's supplementary data archive. Each vibrationally averaged PES was fitted to 578 points, root-mean-square (rms) deviation smaller than 0.1 cm^{-1} , and required only 53 parameters.

2.2. Hamiltonian and matrix elements

Within the Born-Oppenheimer approximation, the rovibrational Hamiltonian of the $\text{H}_2\text{O}-\text{He}$ complex formed from an 'effectively rigid' vibrationally averaged H_2O molecule may be written in the Jacobi coordinate system [55,56]

$$\hat{H} = -\frac{\hbar^2}{2\mu} \frac{\partial^2}{\partial R^2} + \frac{(\hat{J} - \hat{j})^2}{2\mu R^2} + \hat{T}_{\text{H}_2\text{O}} + \Delta\bar{V}(R, \theta, \phi), \quad (2)$$

in which, \hat{J} is the total angular momentum operator for the whole dimer; \hat{j} is the angular momentum operator of H_2O ; μ is the reduced mass of the dimer; $\Delta\bar{V}$ is the intermolecular potential; and $\hat{T}_{\text{H}_2\text{O}}$ stands for the rigid rotor kinetic energy operator for H_2O .

$$\hat{T}_{\text{H}_2\text{O}} = \left(\frac{A+C}{2}\right)\hat{j}_x^2 + \left[B - \left(\frac{A+C}{2}\right)\right]\hat{j}_z^2 + \left(\frac{A-C}{4}\right)(\hat{j}_+^2 + \hat{j}_-^2), \quad (3)$$

where A, B and C are the rotational constants of H_2O with the conventional definition, and $\hat{j}_\pm = \hat{j}_x \mp i\hat{j}_y$.

The total wave function used to solve the Schrödinger equation of $\text{H}_2\text{O}-\text{He}$ complex can be written as a product of radial and angular basis functions using the same approach as in Ref. [56]. In this work, the sine discrete variable representation (DVR) point [57], R_n , are adopted as the basis functions for the radial part. A product of eigenkets of symmetric-top rotations $|jkk\rangle|JKM\rangle$ is used as the elementary angular basis. The details of the frames used in energy levels calculations were shown in Fig. 1(b), $|jkk\rangle$ describes the rotation of the Water-fixed frame (WFF) ($x'-y'-z'$) in the dimer-fixed frame (DFF) ($X'-Y'-Z'$), and $|JKM\rangle$ describes the DFF rotation in the spaced-fixed frame (SFF) ($X-Y-Z$). M is the projection of the total angular momentum J along the SFF Z -axis, and K is the projection of J along the DFF Z' -axis, while k stands for projection of the H_2O angular momentum j onto the WFF z' -axis (the C_2 axis). The $|jkk\rangle$ and $|JKM\rangle$ functions are defined to share the same K value because H_2O is the only source of rotation about the Z' -axis. Our elementary angular basis $|jkk\rangle|JKM\rangle$ can be combined to give a parity-adapted basis [58],

$$|o_{jkk}^{\text{JMP}}\rangle = \frac{1}{\sqrt{2(1+\delta_{k,0}\delta_{K,0})}}[|jkkJKM\rangle + (-1)^{J+K+P}|j-k-KJM\rangle] \quad (4)$$

where the space-inversion parity $P = 0$ or 1 denoting whether the basis is even or odd under inversion. Here, only J and P are rigorously good quantum numbers. The parity of k determines whether H_2O is para or ortho. [59,60,56] Then, the values of $(-1)^{J+P}$ being even or odd gives rovibrational states e or f symmetry, respectively. The eigenvalues and eigenvectors are obtained through the same approach as in Ref. [56]. All states of concern in this work have principal K values of 0 or 1 on the intermolecular axis, denoted as Σ and Π states. For the $j_{k_0k_c}$ assignment, we simply apply the projection operators for the eigenstate into the $|jkk\rangle$ basis. [56] The projection operators $|0_0\rangle\langle 0_0|, |1_{10}\rangle\langle 1_{10}|, |1_{11}\rangle\langle 1_{11}|$ and $|1_{01}\rangle\langle 1_{01}|$ are then used to pick out the corresponding components from the eigenstate. Presently, we use the H_2O ground-state experimental values for the rotational constants ($A = 27.8806 \text{ cm}^{-1}$, $B = 14.5216 \text{ cm}^{-1}$, and $C = 9.2778 \text{ cm}^{-1}$). [61] For the $v_2 = 1$ and $v_3 = 1$ states of H_2O , we choose the A, B, C of H_2O with $v_2 = 1594.746 \text{ cm}^{-1}$ ($A = 31.0847 \text{ cm}^{-1}$, $B = 14.6748 \text{ cm}^{-1}$ and $C = 9.1361 \text{ cm}^{-1}$) [62] and $v_3 = 3755.929 \text{ cm}^{-1}$ ($A = 26.6304 \text{ cm}^{-1}$, $B = 14.4225 \text{ cm}^{-1}$ and $C = 9.1418 \text{ cm}^{-1}$) [63]. The masses of H, O and He atoms were chosen to be 1.00782503207, 15.994915 and 4.002603254u, respectively [64]. In our calculations, we used 50 sine DVR grid points for the R coordinate ranging from $4.0a_0$ to $30.0a_0$. For the angular coordinates, 13 Gaussian-Legendre and 13 Gaussian-Chebyshev quadrature points were used for the numerical integration over θ and ϕ . The treatment of the matrix element of potential $\Delta\bar{V}$ described briefly in the Appendix of Ref. [56].

The transition line strengths between the rovibrational levels can be calculated as [65].

$$S_{i'f} = 3 \sum_{M', M} |\langle \Phi_{i'} | \mu_z^{\text{SFF}} | \Phi_f \rangle|^2 \quad (5)$$

where μ_z^{SFF} stands for the electric dipole operator along the SFF Z -axis and Φ_i is a rovibrational eigenstate. For the $\text{H}_2\text{O}-\text{He}$ dimer, we assume that the dipole moment of the complex is the dipole moment of H_2O . After two steps of rotational coordinate transformation, first from SFF to DFF, and then from DFF to WFF, μ_z^{SFF} can be written as a product of molecular dipole moment $\mu_{\text{H}_2\text{O}}$ with two rotational functions. More details about intensity calculation can be found in Refs. [65,59,56,55].

Assuming that radiation is absorbed by molecules at thermal equilibrium at temperature T , the relative dipole intensity for a transition from a lower state i' to an upper state i is

$$I_{i'f} \propto e^{-E_{i'}/k_B T} \times S_{i'f}, \quad (6)$$

where $E_{i'}$ is the relative energy of lower state $|i'\rangle$.

3. Results and discussion

3.1. Features of the three-dimensional potential energy surface

Fig. 2 presents contour plots of the vibrationally averaged 3D V_{MLR} ground-state potential energy surface for $\text{H}_2\text{O}(0,0,0)-\text{He}$ in Jacobi coordinates. Fig. 2(a) shows how the minimum energy surface depends on θ and R when ϕ is optimized to minimize the energy for each (θ, R) . As seen in Fig. 2(a), the global minimum with a well depth of 34.089 cm^{-1} is located at $(\theta = 76.20^\circ, \phi = 0.0^\circ, R = 3.140 \text{ \AA})$, which is in a planar T-shape geometry with the helium in the H_2O molecular plane ($\phi = 0.0^\circ$). Fig. 2(b) shows how the minimum energy surface depends on θ and ϕ when R is optimized to an energy minimum. As shown in Fig. 2(b), the two equivalent global minima with $\phi = 0.0^\circ$ and $\phi = 180.0^\circ$ (by symmetry), are connected by an out-plane saddle point that is located at $(\theta = 97.40^\circ, \phi = 90.0^\circ$ and $R = 3.567 \text{ \AA})$, with a energy of -14.128 cm^{-1} . Geometries with the helium in

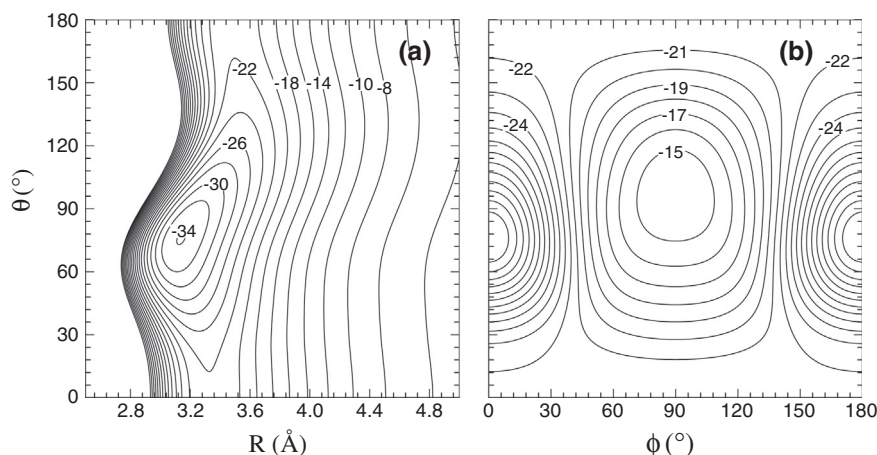


Fig. 2. Contour plots (in cm^{-1}) of the minimum energy surface on our vibrationally averaged 3D $V_{\text{MLR}}(0,0,0)$ PES for $\text{H}_2\text{O}(0,0,0)\text{-He}$: (a) as a function of angle θ and R for optimized value of ϕ , (b) as a function of θ and ϕ for optimized value of R .

the molecular plane ($\phi = 0^\circ$, or 180.0°) are more favorable than out-of-plane structures. Fig. 2(b) also shows that another two in-plane barriers join the two equivalent global minima. One of the in-plane barriers is located at ($R = 3.337 \text{ \AA}$, $\theta = 0^\circ$) with an energy of -21.888 cm^{-1} , and another one is located at ($R = 3.469 \text{ \AA}$, $\theta = 180^\circ$) with an energy of -21.673 cm^{-1} . These two in-plane barriers lie on the C_2 axis, and thus there is no energy dependence on the angle ϕ .

Fig. 3 shows the energy (upper) and radial position (lower) along the minimum-energy path that joins the two in-plane saddle points to the global minimum for $\text{H}_2\text{O-He}$, and compares them with the analogous results for $\text{H}_2\text{O-Ar}$ [45]. As can be seen in Fig. 3(upper), the barriers for in-plane rotation are 12.20 cm^{-1} at $\theta = 0^\circ$ and 12.42 cm^{-1} at $\theta = 180^\circ$. The heights of the barriers are almost equal. It is interesting to notice that the smallest radial position occurs at $\theta = 63.0^\circ$ along the minimum energy path,

which is close to the minimum. For comparison between $\text{H}_2\text{O-He}$ and $\text{H}_2\text{O-Ar}$, the shapes of the radial position curves are very similar to one another, but the difference between the two in-plane saddle-point energies is 6.53 cm^{-1} for $\text{H}_2\text{O-Ar}$, which is significantly larger than that of 0.2 cm^{-1} for $\text{H}_2\text{O-He}$.

The geometries and energies of the global minimum and the saddle points separating them are summarized in Table 1, all of which are compared with previous literature results for this system [37–39]. Overall, our results are consistent with previous *ab initio* surfaces, showing essentially the same anisotropy and similar interaction strength. On our 3D V_{MLR} PES, the well depth at the global minimum recovers 98% of the V_{SAPTH} [37] and V_{SAPTP} [38] well depth, and is 0.289 cm^{-1} deeper than that of the *ab initio* V_{VB} surface [39]. For the vibrationally averaged excited-state (0,1,0) and (0,0,1) surfaces, the contour plots look almost the same as those for the ground state (0,0,0). As shown in Table 1,

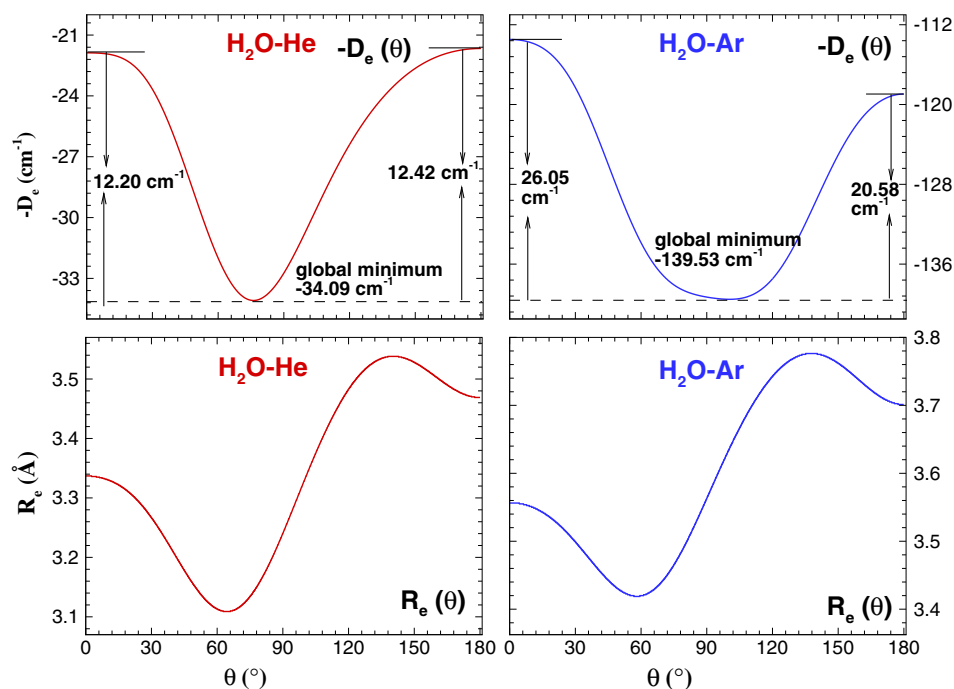


Fig. 3. Energy (upper) and radial position (lower) along the minimum energy path on our vibrationally averaged 3D V_{MLR} PES for $\text{H}_2\text{O}(0,0,0)\text{-He}$ as functions of angle θ for optimized values of ϕ and R .

Table 1

Properties of stationary points on our vibrationally averaged 3D V_{MLR} PESs for the $\text{H}_2\text{O}(\nu_1, \nu_2, \nu_3)\text{-He}$, and comparisons with results from previously reported surfaces. All entries are given as $\{R[\text{\AA}], \theta^\circ, \phi^\circ, \Delta V [\text{cm}^{-1}]\}$, in which some ϕ are given ‘...’, it means that ϕ can be an arbitrary value from 0.0 to 360.0°.

	Global minimum	In-plane saddle-points	Out-plane saddle-point
$V_{\text{MLR}}(0, 0, 0)$	{3.140, 76.2, 0.0, –34.089}	{3.337, 0.0, ..., –21.888} {3.469, 180.0, ..., –21.673}	{3.564, 97.4, 90.0, –14.128}
$V_{\text{MLR}}(0, 1, 0)$	{3.143, 76.0, 0.0, –34.361}	{3.341, 0.0, ..., –21.737} {3.524, 180.0, ..., –20.896}	{3.570, 97.1, 90.0, –14.285}
$V_{\text{MLR}}(0, 0, 1)$	{3.141, 74.3, 0.0, –34.238}	{3.333, 0.0, ..., –22.241} {3.475, 180.0, ..., –21.749}	{3.568, 97.4, 90.0, –14.144}
V_{SAPTH} [37]	{3.12, 78, 0.0, –34.9}	{3.28, 0.0, ..., –21.2}	{3.65, 99, 90, –11.6}
V_{SAPTP} [38]	{3.13, 75, 0.0, –34.9}	{3.52, 180.0, ..., –21.7} {3.34, 0.0, ..., –22.1}	{3.61, 99, 90.0, –13.2}
$V_{\text{CCSD(T)}}$ [39]	{3.19, 79, 0.0, –30.4}	{3.47, 180.0, ..., –21.1} {3.38, 0.0, ..., –18.5}	{3.64, 96, 90.0, –11.5}
V_{MP4} [39]	{3.19, 80, 0.0, –30.0}	{3.48, 180.0, ..., –19.4} {3.40, 0.0, ..., –17.9}	{3.67, 97, 90.0, –10.5}
V_{MP4bf} [39]	{3.14, 77, 0.0, –33.8}	{3.51, 180.0, ..., –18.1} {3.35, 0.0, ..., –20.9}	{3.61, 98, 90.0, –12.7}
V_{VB} [39]	{3.14, 74, 0.0, –33.8}	{3.47, 180.0, ..., –20.5} {3.32, 0.0, ..., –22.7}	{3.53, 90.0, 90.0, –14.3}
		{3.41, 180.0, ..., –23.0}	

the positions and energies of the stationary points are only slightly shifted.

3.2. Bound states and band origin shifts

The calculated rovibrational energy levels with $(\nu_1, \nu_2, \nu_3) = (0, 0, 0)$, $(0, 1, 0)$, and $(0, 0, 1)$ are listed in Table 2 for *para*- H_2O -He and *ortho*- H_2O -He. The rovibrational energy levels are labeled with six quantum numbers $(J, j_{k_q k_c}, K, k, P, n_s)$ in a free internal rotor model, where J is the total angular momentum for the whole complex, $j_{k_q k_c}$ denotes the asymmetric top level of the H_2O subunit, K is the projection of J on the intermolecular axis, where $K = 0$ or $K = 1$ are corresponding to Σ or Π state, k is the projection of j on the C_2 axis of the H_2O molecule in which the

Table 2

Calculated energies (in cm^{-1}) for the rovibrational levels from our vibrationally averaged 3D V_{MLR} PESs for $\text{H}_2\text{O}(\nu_1, \nu_2, \nu_3)\text{-He}$, which are expressed relative to the relevant asymptote. The * means resonance states (labeled with $K(j_{k_q k_c})^{P+J}$).

	$J = 0$	$J = 1$	$J = 2$	$J = 3$	$J = 4$
<i>para</i> - $\text{H}_2\text{O}(0,0,0)\text{-He}$					
$\Sigma(0_{00})^e$	–6.758	–6.083	–4.750	–2.801	–0.323
* $\Pi(1_{11})^e$		30.370	31.030	32.330	34.216
$\Pi(1_{11})^f$		31.079	32.417	34.373	36.859
<i>ortho</i> - $\text{H}_2\text{O}(0,0,0)\text{-He}$					
$\Sigma(1_{01})^e$	16.170	16.417	17.203	18.610	20.627
$\Pi(1_{01})^e$		18.876	20.749	23.205	
$\Pi(1_{01})^f$		18.429	19.720	21.600	
<i>para</i> - $\text{H}_2\text{O}(0,1,0)\text{-He}$					
$\Sigma(0_{00})^e$	–6.758	–6.084	–4.754	–2.809	–0.335
* $\Pi(1_{11})^e$		33.750	34.400	35.588	37.434
$\Pi(1_{11})^f$		34.128	35.464	37.418	39.902
<i>ortho</i> - $\text{H}_2\text{O}(0,1,0)\text{-He}$					
$\Sigma(1_{01})^e$	16.170	16.421	17.207	18.613	20.627
$\Pi(1_{01})^e$		18.888	20.755	23.205	
$\Pi(1_{01})^f$		18.445	19.733	21.610	
<i>para</i> - $\text{H}_2\text{O}(0,0,1)\text{-He}$					
$\Sigma(0_{00})^e$	–6.782	–6.112	–4.789	–2.854	–0.390
* $\Pi(1_{11})^e$		29.047	29.711	30.985	32.859
$\Pi(1_{11})^f$		29.637	30.967	32.913	35.390
<i>ortho</i> - $\text{H}_2\text{O}(0,0,1)\text{-He}$					
$\Sigma(1_{01})^e$	15.928	16.169	16.946	18.342	20.343
$\Pi(1_{01})^e$		18.598	20.462	22.905	
$\Pi(1_{01})^f$		18.151	19.435	21.305	

evenness and oddness of k determines whether they apply to a *para*- H_2O -He or *ortho*- H_2O -He complex, $P = 0$ or 1 stands for the space-inversion parity, and n_s is the radial stretching quantum number.

Table 2 lists the energies of the ($J = 0 - 4$) intermolecular rovibrational energy levels for *para*- H_2O -He and *ortho*- H_2O -He generated from our 3D V_{MLR} PESs, and the Fig. 4 shows the schematic rotational energy level diagram for *para*- H_2O -He and *ortho*- H_2O -He with $(\nu_1, \nu_2, \nu_3) = (0, 0, 0)$. On this scale energies of the excited $\nu_2 = 1$ and $\nu_3 = 1$ states would be almost identical.

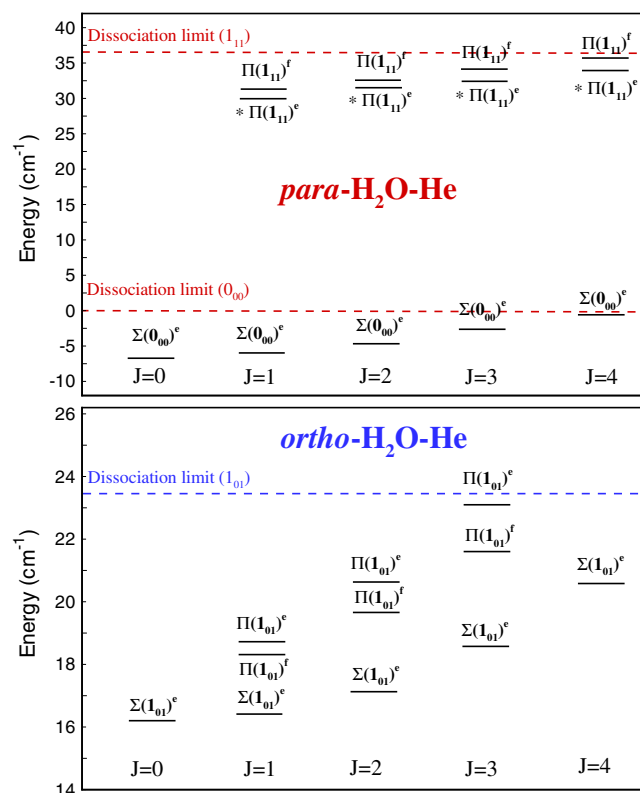


Fig. 4. Schematic rotational energy level diagram (labeled with $K(j_{k_q k_c})^{P+J}$) for *para*- H_2O -He and *ortho*- H_2O -He with $(\nu_1, \nu_2, \nu_3) = (0, 0, 0)$. For *para*- H_2O -He, the dissociation limit of 0₀₀ is 0.0 cm^{-1} and 1₁₁ is 37.137 cm^{-1} . For *ortho*- H_2O -He, the dissociation limit of 1₀₁ is 23.794 cm^{-1} .

Table 3

The lowest energies (in cm^{-1}) for the rovibrational levels of our vibrationally averaged 3D V_{MLR} PESs for H_2O (0,0,0)-Rg(He, Ne [66], Ar [45]) (labeled with $K(j_{ka}k_c)^{p-i,j}$), and the band origin shifts associated with three fundamental bands of ν_1 , ν_2 and ν_3 of *para*- H_2O -Rg and *ortho*- H_2O -Rg, respectively.

	H_2O -He	H_2O -Ne [66]	H_2O -Ar [45]
$\Sigma(0_{00})^e$	-6.758	-31.908	-93.494
$\Pi(1_{11})^e$	30.370	5.416	-56.433
$\Pi(1_{11})^f$	31.079	5.481	-59.421
$\Sigma(1_{01})^e$	16.170	-11.417	-76.646
$\Pi(1_{01})^e$	18.876	-5.908	-65.229
$\Pi(1_{01})^f$	18.429	-5.939	-65.236
<i>para</i> - H_2O -Rg			
$\Delta\nu_1$	0.039		-1.675
$\Delta\nu_2$	0.000	-0.059	-0.671
$\Delta\nu_3$	-0.025		-1.999
<i>ortho</i> - H_2O -Rg			
$\Delta\nu_1$	-0.257		-2.236
$\Delta\nu_2$	0.000	-0.108	-0.913
$\Delta\nu_3$	-0.242		-2.506

Table 4

The Global minimum, saddle point and dissociation energy (D_0) (in cm^{-1}) for H_2O -He, which compared with other H_2O -Ne [66], H_2O -Ar [45], H_2O -Kr [67], H_2O -Xe [68], CO-He [23,24], C_2D_2 -He [69,25] and HCN-He [72] systems.

	Global minimum	Saddle point	D_0	
			<i>para</i> - H_2O -Rg	<i>ortho</i> - H_2O -Rg
H_2O -He	-34.089	-21.888	6.758	7.629
H_2O -Ne	-64.295	-48.576	30.908	35.216
H_2O -Ar	-139.529	-113.477	93.494	100.445
H_2O -Kr	-169.98	-145.72	119.461	127.06
H_2O -Xe	-192.5	-169.2	139.937	147.14
CO-He	-22.910		6.5	
C_2D_2 -He	-24.21	-16.7	7.236	
HCN-He	-30.2	-21.3	9.420	

Table 3 shows the values for the lowest energies levels for H_2O -He, which compared with those of H_2O -Ne [66] and H_2O -Ar [45]. The values of energy level exhibit that the spectrum for H_2O -He is the more difficult to be observed than those for H_2O -Ar and H_2O -Ne. For *para*- H_2O -He, -6.758 cm^{-1} is the lowest rovibrational energy for the ground state which indicates that the zero-point energy is 27.331 cm^{-1} , about 80% of the global well depth D_e (34.089 cm^{-1}). As shown in Table 4, the global minimum, saddle point and dissociation energies for H_2O -He are compared with H_2O -Ne [66], H_2O -Ar [45], H_2O -Kr [67], H_2O -Xe [68], CO-He [23,24] and C_2D_2 -He [69,25] systems. The dissociation energy is 6.758 cm^{-1} for *para*- H_2O -He which approaches to the 6.5 cm^{-1} for the CO-He [24] system and 7.236 cm^{-1} for the C_2D_2 -He [25] complex, and the values of dissociation energies illuminate that the spectrum of H_2O -He is likely to be observed. The zero-point energy of *para*- H_2O -He is significantly higher than the in-plane barriers of 12.20 and 12.42 cm^{-1} , which indicates that the ground-state wave function is highly delocalized.

For *ortho*- H_2O -He, the energies of the bound states should be lower than the asymptote of *ortho*- H_2O with $j_{ka}k_c = 1_{01}$ with energy of 23.794 cm^{-1} , which calculated from the sum of the rotational constants $B + C$ of H_2O . As seen in Table 2, the lowest bound state has an energy of 16.170 cm^{-1} , so the dissociation energy is 7.629 cm^{-1} for *ortho*- H_2O -He, which is about 1 cm^{-1} larger than the 6.758 cm^{-1} dissociation energy of *para*- H_2O -He. Therefore, *ortho*- H_2O -He is more stable than *para*- H_2O -He. The similar trend have been found for H_2O -Ar system [45], the dissociation energy of *ortho*- H_2O -Ar is larger than that of *para*- H_2O -Ar.

The wave functions for the lowest energy levels of *para*- H_2O -He and *ortho*- H_2O -He are shown in Figs. 5 and 6. Comparison of the wave functions for *para*- H_2O -He with those for *ortho*- H_2O -He shows that the main difference is the wave function along the ϕ coordinate. The *para*- H_2O -He bound-state wave function exhibits very little variation with ϕ , which is expected, due to the low

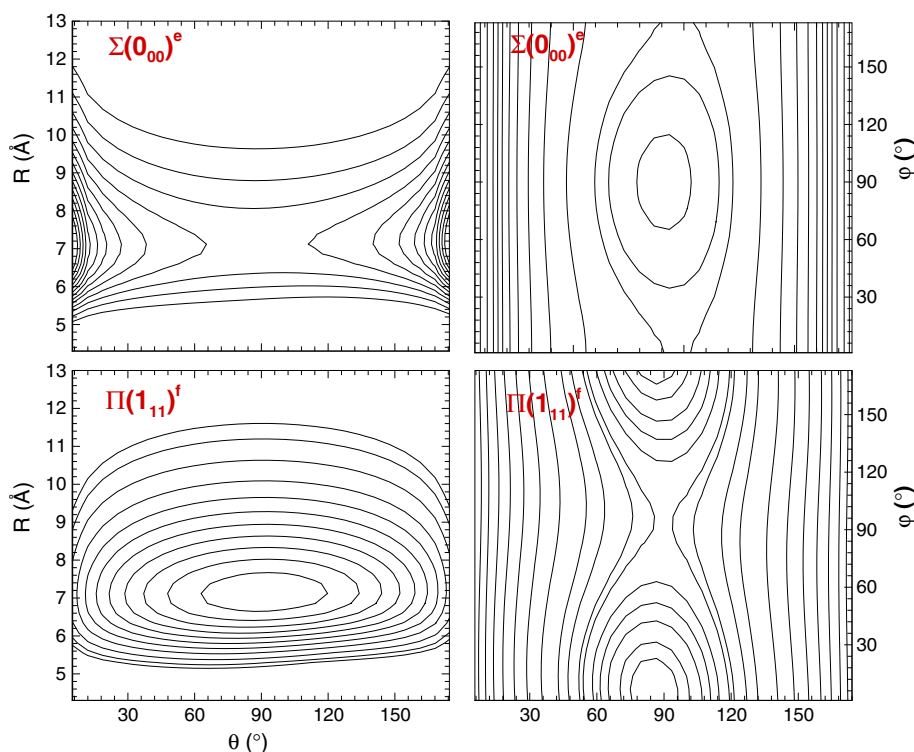


Fig. 5. Wave functions for the lowest energy levels of *para*- H_2O -He: (left) as a function of R and θ , (right side) as a function of θ and ϕ , respectively.

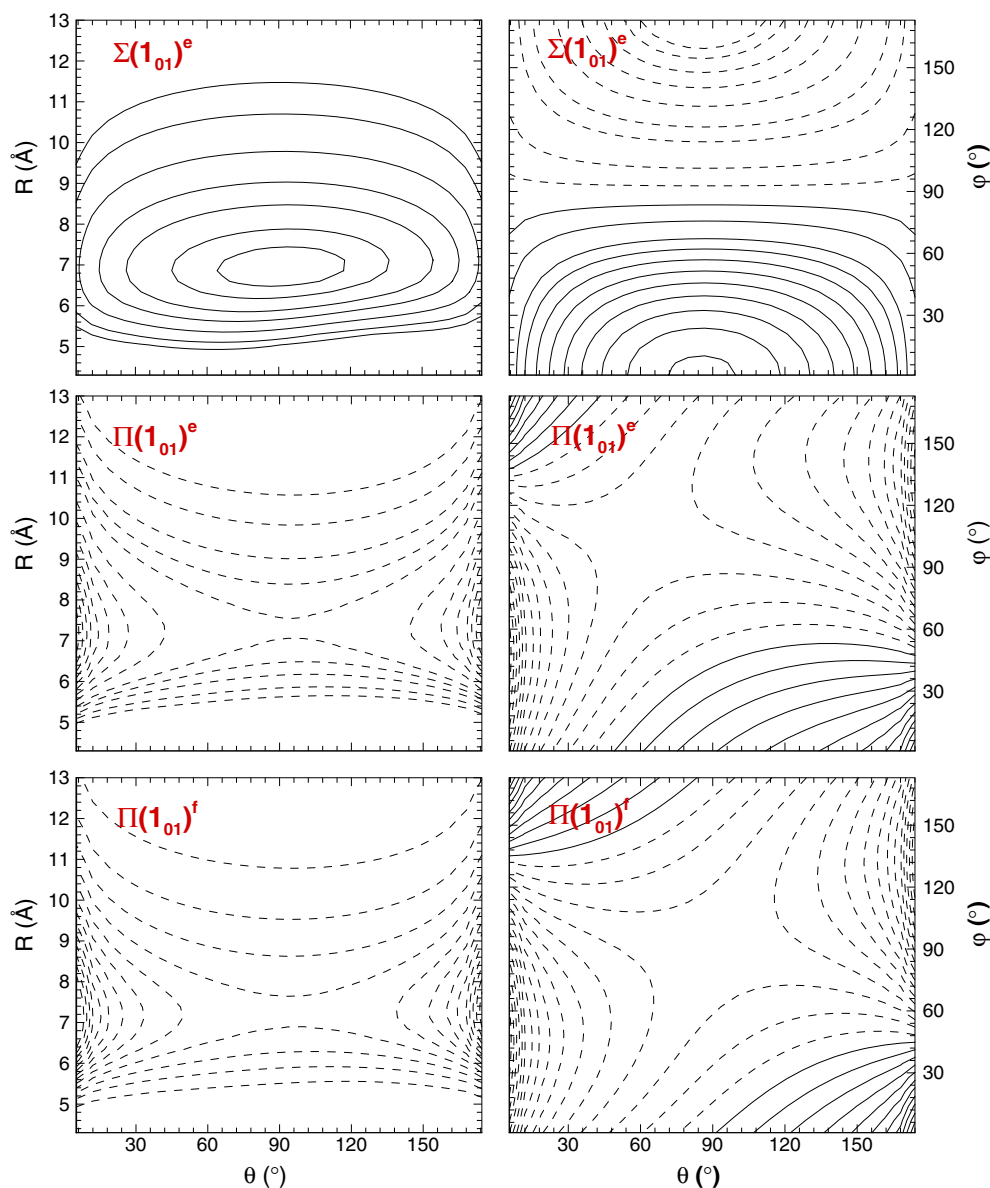


Fig. 6. Wave functions for the lowest energy levels of *ortho*-H₂O-He: (left) as a function of R and θ , (right side) as a function of θ and ϕ , respectively.

potential-energy barrier in the ϕ direction. However, for *ortho*-H₂O-He, the bound-state wave function exhibits a clear nodal structure and substantial variation along the ϕ coordinate. For *para*-H₂O-He, the analysis of the wave function indicates that the $\Pi(1_{11})^e$ is a resonance state, and the $\Pi(1_{11})^e$ state has 62%, 55%, 52% and 47% of Π -contribution for $J = 1, 2, 3$ and 4. However, the corresponding $\Pi(1_{11})^f$ state has 99% of Π -contribution for $J = 1 - 4$. For *ortho*-H₂O-He $\Pi(1_{01})$ states, the wave functions of e and f symmetry are similar to each other, except for a slight shift along the θ and ϕ coordinates.

The band origin shifts associated with three fundamental modes of ν_1, ν_2 , and ν_3 of H₂O-Rg(He, Ne, Ar) are predicted from our vibrationally averaged 3D V_{MLR} PESs, which are exhibited in Table 3. For all of the ν_1, ν_2 and ν_3 modes, the shifts for the H₂O-Ar [45] system are significantly larger than the corresponding values for H₂O-Ne [66] and H₂O-He. The predicted $\Delta\nu_3$ shifts are -0.0246 cm^{-1} and -0.2417 cm^{-1} for *para*-H₂O-He and *ortho*-H₂O-He, both being red shifts. In contrast, the predicted $\Delta\nu_2$ shifts are -0.0005 and -0.0004 cm^{-1} for *para*-H₂O-He and *ortho*-H₂O-He, respectively. The energy levels for H₂O-He do not account for

the very small $\Delta\nu_2$ shifts that arise from the fact which He is interacting with the vibrationally excited ν_2 of H₂O. All predicted shifts of *ortho*-H₂O-He are larger than the corresponding values of *para*-H₂O-He, due to stronger binding energy of *ortho*-H₂O-He than that of *para*-H₂O-He.

3.3. Predicted microwave and infrared spectra and their transition intensities

In Table 5, we report line strengths of rotational transitions for *para*-H₂O-He and *ortho*-H₂O-He on the $(\nu_1, \nu_2, \nu_3) = (0, 0, 0)$ H₂O-He PES that was obtained by averaging over the full-dimension $\Delta V(R, \theta, \phi, Q_1, Q_2, Q_3)$ intermolecular potential. The rotational levels were assigned using the labels $J, j_{K_a K_c}$ and K , as discussed in Section 3.2. We choose to present R-branch results because all bands have an R(1) transition. The P(1) transitions are not as good for intensity comparisons because there are no $J = 0 \Pi$ states, and Q(1) transition are not appropriate because a $\Sigma \rightarrow \Sigma$ band does not have a Q branch [59]. As shown in Table 5, we find that there only exist $\Sigma \rightarrow \Sigma$ type transitions for

Table 5

Line strengths for microwave lines between bound states of H₂O-He, each level is labeled with its assignment (labeled with $K(j_{ka,ke})^{P+J}$) and energy (cm⁻¹), line strength values are multiplied by 10⁵.

	$J'-J''$	E'	E''	Cal.	Line strength
<i>para</i> -H ₂ O-He					
$\sum(0_{00})^e \leftarrow \sum(0_{00})^e$	1-0	-6.083	-6.758	0.675	1.3
	2-1	-4.750	-6.083	1.333	1.2
	3-2	-2.801	-4.750	1.949	0.1
	4-3	-0.323	-2.801	2.478	1.8
$\Pi(1_{11})^f \leftarrow \Pi(1_{11})^f$	2-1	32.417	31.079	1.338	1.0
	3-2	34.373	32.417	1.956	0.5
	4-3	36.859	34.373	2.486	0.0
<i>ortho</i> -H ₂ O-He					
$\sum(1_{01})^e \leftarrow \sum(1_{01})^e$	1-0	16.417	16.170	0.248	0.6
	2-1	17.203	16.417	0.785	3.2
	3-2	18.610	17.203	1.408	3.8
	4-3	20.627	18.610	2.017	1.4
$\Pi(1_{01})^e \leftarrow \sum(1_{01})^e$	1-0	18.876	16.170	2.707	5.6
	2-1	20.749	16.417	4.332	4.2
	3-2	23.205	17.203	6.003	2.9
$\Pi(1_{01})^e \leftarrow \Pi(1_{01})^e$	2-1	20.720	18.876	1.874	0.0
	3-2	23.205	20.720	2.456	3.7
$\Pi(1_{01})^f \leftarrow \Pi(1_{01})^f$	2-1	19.720	18.429	1.291	0.2
	3-2	21.600	19.720	1.880	1.3

para-H₂O-He. For *ortho*-H₂O-He, the largest strengths are 3.8×10^{-5} for R(2) of $\sum(1_{01})^e \rightarrow \sum(1_{01})^e$, 5.6×10^{-5} for R(0) of $\Pi(1_{01})^e \rightarrow \sum(1_{01})^e$ and 3.7×10^{-5} for R(2) of $\Pi(1_{01})^e \rightarrow \Pi(1_{01})^e$, respectively. However, the strengths of all *para*-H₂O-He and *ortho*-H₂O-He bands are much weaker than those for H₂O-*para*H₂

Table 6

Predicted infrared (ν_1, ν_2, ν_3) = (0, 1, 0) \leftarrow (0, 0, 0) transitions (in cm⁻¹), line strengths, and relative intensities at temperature of 5.0 K for H₂O-He from our vibrationally averaged 3D $V_{\text{MLR}}(R, \theta, \phi)$ PESs. The line strength values are multiplied by 10⁵ (labeled with $K(j_{ka,ke})^{P+J}$).

Levels $J'-J''$	Cal.	Line strength	Intensity 5 K
$\sum(0_{00})^e \leftarrow \sum(0_{00})^e$			
0-1	1594.071	1.3	0.826
1-2	1593.412	1.1	0.495
2-3	1592.793	0.1	0.015
3-4	1592.261	1.6	0.202
1-0	1595.420	1.3	1.000
2-1	1596.075	1.1	0.724
3-2	1596.687	0.1	0.027
4-3	1597.212	1.6	0.400
$\Pi(1_{11})^f \leftarrow \sum(0_{00})^e$			
1-1	1634.957	1.0×10^5	0.881
2-2	1634.960	1.7×10^5	1.000
3-3	1634.965	2.3×10^5	0.799
4-4	1634.971	3.0×10^5	0.503
$\Pi(1_{01})^e \leftarrow \sum(1_{01})^e$			
1-0	1597.465	5.2	0.831
2-1	1598.612	4.4	0.662
3-2	1600.749	3.5	0.412
4-3	1600.895	0.8	0.062
1-2	1596.432	0.9	0.109
2-3	1596.892	0.0	0.001
3-4	1597.325	5.4	0.239
1-1	1596.775	6.7	1.000
2-2	1597.277	3.8	0.455
3-3	1597.746	0.3	0.023
$\Pi(1_{01})^f \leftarrow \Pi(1_{01})^f$			
1-2	1593.472	0.1	0.072
2-3	1592.879	1.4	0.633
2-1	1596.051	0.1	0.106
3-2	1596.636	1.3	1.000
1-1	1594.316	0.0	0.029
2-2	1593.730	1.1	0.668
3-3	1593.151	1.4	0.420

Table 7

Predicted infrared (ν_1, ν_2, ν_3) = (0, 0, 1) \leftarrow (0, 0, 0) transitions (in cm⁻¹), line strengths, and relative intensities at temperature of 5.0 K for H₂O-He from our vibrationally averaged 3D $V_{\text{MLR}}(R, \theta, \phi)$ PESs. The line strength values are multiplied by 10⁵ (labeled with $K(j_{ka,ke})^{P+J}$).

Levels $J'-J''$	Cal.	Line strength	Intensity 5 K
$\Pi(1_{01})^e \leftarrow \sum(0_{00})^e$			
1-2	3779.277	8.6	0.147
2-3	3779.191	4.2	0.041
3-4	3779.157	0.5	0.002
1-0	3781.285	33.0	1.000
2-1	3782.473	29.6	0.739
3-2	3783.584	9.9	0.168
1-1	3780.162	29.2	0.729
2-2	3780.113	12.0	0.204
3-3	3780.035	1.0	0.010
4-4	3779.915	7.5	0.036
$\Pi(1_{11})^f \leftarrow \Pi(1_{01})^e$			
1-2	3765.846	0.9×10^4	0.108
2-3	3765.295	0.8×10^4	0.051
1-1	3766.689	7.0×10^4	1.000
2-2	3766.146	3.9×10^4	0.325
3-3	3765.636	2.7×10^4	0.113
$\sum(0_{00})^e \leftarrow \Pi(1_{01})^e$			
0-1	3730.270	14.2	1.000
1-2	3729.067	9.7	0.399
2-3	3727.934	0.7	0.014
3-4	3728.327	9.2	0.119
2-1	3732.264	3.6	0.256
3-2	3732.325	0.9	0.035
4-3	3732.333	2.6	0.052
1-1	3731.387	11.4	0.911
2-2	3731.420	1.7	0.094
3-3	3731.475	7.7	0.248

[59], which explains why it is so difficult to observe the spectrum of H₂O-He.

For ν_2 or ν_3 transitions, the predicted infrared (IR) transition frequencies (cm⁻¹) from our 3D- V_{MLR} potential are listed in Tables 6 and 7, respectively. For infrared transitions, we calculate the IR rovibrational transitions from:

$$\nu_2 = \nu_2(\text{H}_2\text{O}) + E_{\nu_2=1}^{\text{upper}} - E_{\nu_2=0}^{\text{lower}} \quad (7)$$

$$\nu_3 = \nu_3(\text{H}_2\text{O}) + E_{\nu_3=1}^{\text{upper}} - E_{\nu_3=0}^{\text{lower}} \quad (8)$$

where, $\nu_2(\text{H}_2\text{O}) = 1594.7463$ cm⁻¹ [62] and $\nu_3(\text{H}_2\text{O}) = 3755.9287$ cm⁻¹ [63] are the experimental fundamental bend region and asymmetric-stretch vibrational transition frequencies of a free H₂O molecule, respectively (see Fig. 7).

As shown in Table 6, the infrared $\nu_2 = 1 \leftarrow 0$ transitions of *para*-H₂O-He is $\sum(0_{00})^e \leftarrow \sum(0_{00})^e$ and $\Pi(1_{11})^f \leftarrow \sum(0_{00})^e$, and *ortho*-H₂O-He are $\Pi(1_{01})^e \leftarrow \sum(1_{01})^e$ and $\Pi(1_{01})^f \leftarrow \Pi(1_{01})^f$ (labeled with $K(j_{ka,ke})^{P+J}$). To select most possible IR transitions of H₂O-He, the relative intensities at temperature 5.0 K are calculated, and expressed relative to the strongest transitions of $J = 0 \leftarrow 1$ for $\sum(0_{00})^e \leftarrow \sum(0_{00})^e$, $J = 2 \leftarrow 2$ for $\Pi(1_{11})^f \leftarrow \sum(0_{00})^e$, $J = 1 \leftarrow 0$ for $\Pi(1_{01})^e \leftarrow \sum(1_{01})^e$ and $J = 3 \leftarrow 2$ for $\Pi(1_{01})^f \leftarrow \Pi(1_{01})^f$, whose intensities are set to 1. Especially, the line strengths of transitions with $\Pi(1_{11})^f \leftarrow \sum(0_{00})^e$ are five orders of magnitude larger than the other transitions which may make them more easily to be observed. The same situation is also found in H₂O-Ne system [66], the line strengths of transitions with $\Pi(1_{11})^f \leftarrow \sum(0_{00})^e$ are two orders of magnitude larger than the other transitions for *para*-H₂O-Ne. With line strength larger than $10^{-3}(u_{\text{H}_2\text{O}}^2)$, column 4 of Table 6 lists the relative intensities for a total of 31 transitions, including P, Q, and R branch patterns and

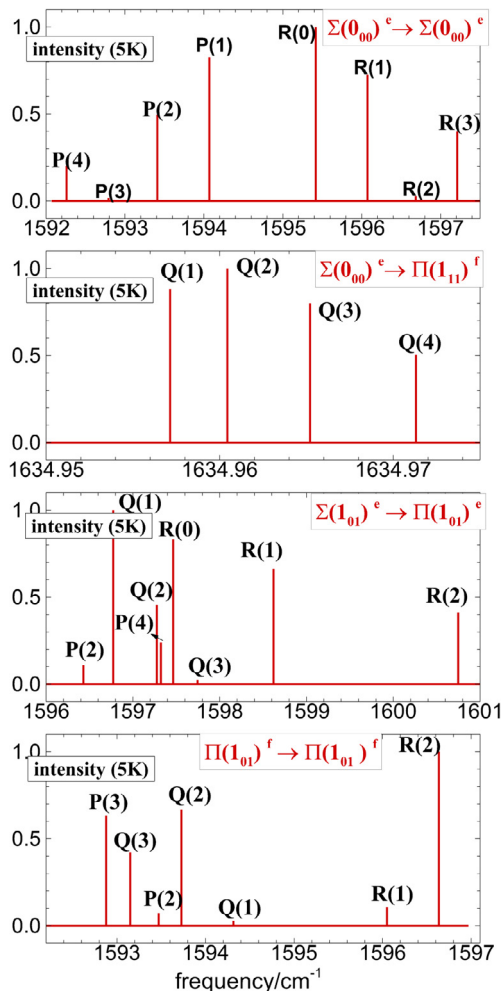


Fig. 7. Calculated infrared spectra of $\nu_2 = 1 \leftarrow 0$ for $\text{H}_2\text{O-He}$, shown with relative intensity at 5.0 K. The intensities of *para*- $\text{H}_2\text{O-He}$ are expressed relative to $J = 0 \leftarrow 1$ for $\Sigma(0_{00})^e \leftarrow \Sigma(0_{00})^e$ and $J = 2 \leftarrow 2$ for $\Pi(1_{11})^f \leftarrow \Sigma(0_{00})^e$. The intensities of *ortho*- $\text{H}_2\text{O-He}$ are expressed relative to $J = 1 \leftarrow 0$ for $\Pi(1_{01})^e \leftarrow \Sigma(1_{01})^e$ and $J = 3 \leftarrow 2$ for $\Pi(1_{01})^f \leftarrow \Pi(1_{01})^f$.

column 2 is ν_2 transitions. Fig. 8 shows the relative strengths of the $\Pi(1_{11})^f \leftarrow \Sigma(0_{00})^e$ band for *para*- $\text{H}_2\text{O-He}$, Ne [66] and Ar [45], which expressed relative to Q_1 transition of $1634.9571 \text{ cm}^{-1}$ for *para*- $\text{H}_2\text{O-He}$, $1634.8130 \text{ cm}^{-1}$ for *para*- $\text{H}_2\text{O-Ne}$ and $1634.0245 \text{ cm}^{-1}$ for *para*- $\text{H}_2\text{O-Ar}$, respectively. In Fig. 8, the $\Pi(1_{11})^f \leftarrow \Sigma(0_{00})^e$ band are the red shifts for *para*- $\text{H}_2\text{O-Rg}$ complexes, and the line spacing between the rotational lines for *para*- $\text{H}_2\text{O-He}$ are the biggest, due to the weakest inter-molecular interaction among three systems.

For $\nu_3 = 1 \leftarrow 0$ transitions, the calculated infrared transition frequencies expressed relative to the band origin $3755.9287 \text{ cm}^{-1}$ of a free H_2O monomer are predicted in Table 7. Column 4 of Table 7 expresses all the relative intensities at temperature 5.0 K relative to the transitions of $J = 1 \leftarrow 0$ for $\Pi(1_{01})^e \leftarrow \Sigma(0_{00})^e$, $J = 1 \leftarrow 1$ for $\Pi(1_{11})^f \leftarrow \Pi(1_{01})^e$ of *para*- $\text{H}_2\text{O-He}$ and $J = 0 \leftarrow 1$ for $\Sigma(0_{00})^e \leftarrow \Pi(1_{01})^e$ of *ortho*- $\text{H}_2\text{O-He}$. A total of 25 relative intensities are presented in Table 7 and Fig. 9. As seen in the last column of Table 7, the $J = 1 \leftarrow 0$, $J = 2 \leftarrow 1$, $J = 1 \leftarrow 1$ and $J = 2 \leftarrow 2$ for $\Pi(1_{01})^e \leftarrow \Sigma(0_{00})^e$, $J = 0 \leftarrow 1$ for $\Sigma(0_{00})^e \leftarrow \Pi(1_{01})^e$ and all transitions for $\Pi(1_{11})^f \leftarrow \Pi(1_{01})^e$ have relative stronger line strengths and intensities at 5 K, which may be observed transitions in future experimental studies.

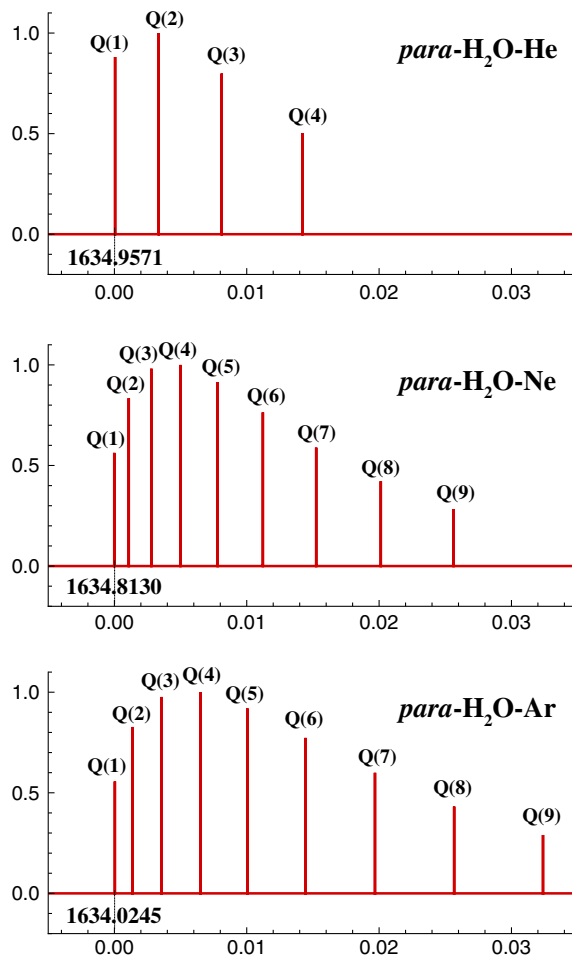


Fig. 8. The relative intensities of *para*- $\text{H}_2\text{O-He}$, *para*- $\text{H}_2\text{O-Ne}$ and *para*- $\text{H}_2\text{O-Ar}$ are compared with each other for $\Pi(1_{11})^f \leftarrow \Sigma(0_{00})^e$ band.

4. Conclusion

In this paper, we have presented an accurate $\text{H}_2\text{O-He}$ potential energy surface that includes an explicit dependence on the Q_1 , Q_2 and Q_3 normal coordinates of the H_2O molecule. This potential energy surface is based on *ab initio* interaction energies obtained at the CCSD(T) level with a large aug-cc-pVQZ basis set and with bond functions placed at the mid-point on the intermolecular axis. The vibrationally averaged potential energies were fitted to a 3D Morse/Long-Range (MLR) potential form that incorporates the theoretically known long-range inverse-power behavior [70,71,55]; having this correct long-range behavior is very important and necessary to provide a good fundament of studying H_2O collision with He in astrophysical and atmospheric environment. The global 3D fit to the 578 vibrationally averaged interaction energies had a rms deviation smaller than 0.1 cm^{-1} , and required only 53 parameters each.

The PESs have been employed to compute the rovibrational energy levels for *para*- $\text{H}_2\text{O-He}$ and *ortho*- $\text{H}_2\text{O-He}$ complexes using the radial DVR/angular FBR method. The calculated band origin shifts on a full 6D-dimension intra- and intermolecular PES associated with three fundamental transitions of H_2O for both *para*- $\text{H}_2\text{O-He}$ and *ortho*- $\text{H}_2\text{O-He}$ were predicted for the first time. In addition, we first presented the microwave and infrared spectra of *para*- $\text{H}_2\text{O-He}$ and *ortho*- $\text{H}_2\text{O-He}$ on the vibrationally quantum-state-specific PESs. Especially, the line strengths of transitions with

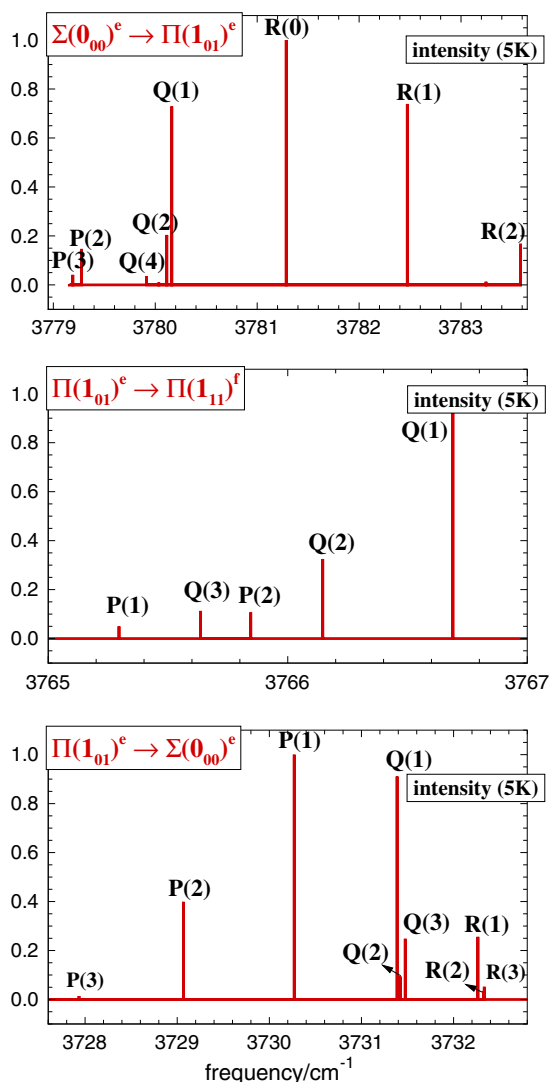


Fig. 9. Calculated infrared spectra of $\nu_3 = 1 \leftarrow 0$ for $\text{H}_2\text{O-He}$, shown with relative intensity at 5.0 K. The intensities of *para*- $\text{H}_2\text{O-He}$ are expressed relative to $J = 1 \leftarrow 0$ for $\Pi(1_{01})^e \leftarrow \Sigma(0_{00})^e$ and $J = 1 \leftarrow 1$ for $\Pi(1_{11})^f \leftarrow \Pi(1_{01})^e$. The intensities of *ortho*- $\text{H}_2\text{O-He}$ are expressed relative to $J = 0 \leftarrow 1$ for $\Sigma(0_{00})^e \leftarrow \Pi(1_{01})^e$.

$\Pi(1_{11})^f \leftarrow \Sigma(0_{00})^e$ for *para*- $\text{H}_2\text{O-He}$ and $\Pi(1_{11})^f \leftarrow \Pi(1_{01})^e$ for *ortho*- $\text{H}_2\text{O-He}$ are more considerable than the other transitions which may make those bands more easily to be observed.

Acknowledgments

We are grateful to Professor Robert J. Le Roy for helpful discussions and thoughtful comments on our manuscript. This research has been supported by the National Natural Science Foundation of China (Grant Nos. 21273094, 21533003 and 91541124), Program for New Century Excellent Talents in University, and Beijing National Laboratory for Molecular Sciences (BNLMS).

Appendix A. Supplementary material

Supplementary data associated with this article can be found, in the online version, at <http://dx.doi.org/10.1016/j.jms.2016.07.009>.

References

- [1] B.H. Yang, P.C. Stancil, J. Chem. Phys. 126 (2007) 154306, <http://dx.doi.org/10.1063/1.2720390>.
- [2] B.H. Yang, M. Nagao, M.K.W. Satomi, P.C. Stancil, Astrophys. J. 765 (2013) 77, <http://dx.doi.org/10.1088/0004-637X/765/2/77>.
- [3] R.T.V. Kung, R.E. Center, J. Chem. Phys. 62 (1975) 2187–2194, <http://dx.doi.org/10.1063/1.430786>.
- [4] P. Wannier, L. Pagani, T. Kuiper, M. Frerking, S. Gulkis, P. Encrenaz, H. Pickett, A. Lecacheux, W. Wilson, Astrophys. J. 377 (1991) 177–186.
- [5] G. Melnick, J. Stauffer, M. Ashby, E. Bergin, G. Chin, N. Erickson, P. Goldsmith, M. Harwit, J. Howe, S. Kleiner, D. Koch, D. Neufeld, B. Patten, R. Plume, R. Schieder, R. Snell, V. Tolls, Z. Wang, G. Winnewisser, Y.-F. Zhang, The submillimeter wave astronomy satellite: science objectives and instrument description, Astrophys. J. 539 (2000) L77–L85.
- [6] R.C. Cohen, K.L. Busarow, K.B. Laughlin, G.A. Blake, M. Havenith, Y.T. Lee, R.J. Saykally, J. Chem. Phys. 89 (1988) 4494–4504, <http://dx.doi.org/10.1063/1.454789>.
- [7] R.C. Cohen, K.L. Busarow, Y.T. Lee, R.J. Saykally, J. Chem. Phys. 92 (1990) 169–177, <http://dx.doi.org/10.1063/1.458459>.
- [8] R.C. Cohen, R.J. Saykally, J. Chem. Phys. 98 (1993) 6007–6030, <http://dx.doi.org/10.1063/1.464841>.
- [9] T.C. Germann, H.S. Gutowsky, J. Chem. Phys. 98 (1993) 5235–5238, <http://dx.doi.org/10.1063/1.464923>.
- [10] R.C. Cohen, R.J. Saykally, J. Chem. Phys. 95 (1991) 7891–7906, <http://dx.doi.org/10.1063/1.461318>.
- [11] S. Suzuki, R.E. Bumgarner, P.A. Stockman, P.G. Green, G.A. Blake, J. Chem. Phys. 94 (1991) 824–825, <http://dx.doi.org/10.1063/1.460308>.
- [12] G.T. Fraser, F.J. Lovas, R.D. Suenram, K. Matsumura, J. Mol. Spectrosc. 144 (1990) 97, [http://dx.doi.org/10.1016/0022-2852\(90\)90310-M](http://dx.doi.org/10.1016/0022-2852(90)90310-M).
- [13] R. Lascola, D.J. Nesbitt, J. Chem. Phys. 95 (1991) 7917–7932, <http://dx.doi.org/10.1063/1.461320>.
- [14] D.J. Nesbitt, R. Lascola, J. Chem. Phys. 97 (1992) 8096–8110, <http://dx.doi.org/10.1063/1.463431>.
- [15] M.J. Weida, D.J. Nesbitt, J. Chem. Phys. 106 (1997) 3078–3089, <http://dx.doi.org/10.1063/1.473051>.
- [16] X.-C. Liu, Y.-J. Xu, J. Mol. Spectrosc. 301 (2014) 1–8, <http://dx.doi.org/10.1016/j.jms.2014.04.005>.
- [17] K. Didriche, T. Földes, J. Chem. Phys. 138 (2013) 104307, <http://dx.doi.org/10.1063/1.4794161>.
- [18] Q. Wen, W. Jäger, J. Phys. Chem. A 110 (2006) 7560–7567, <http://dx.doi.org/10.1021/jp0619890>.
- [19] J. van Wijngaarden, W. Jäger, Mol. Phys. 98 (2000) 1575–1588, <http://dx.doi.org/10.1080/00268970009483363>.
- [20] S. Li, R. Zheng, Y. Zhu, C.X. Duan, J. Chem. Phys. 135 (2011) 134304.
- [21] K.E. Kuyanov, M.N. Slipchenko, A.F. Vilesov, Chem. Phys. Lett. 427 (2006) 5–9, <http://dx.doi.org/10.1016/j.cplett.2006.05.134>.
- [22] C. Lindsay, G. Doublerly, R. Miller, J. Mol. Struct. 786 (2006) 96–104, <http://dx.doi.org/10.1016/j.molstruc.2005.09.025>.
- [23] C.E. Chuaqui, R.J.L. Roy, A.R.W. McKellar, J. Chem. Phys. 101 (1994) 39–61, <http://dx.doi.org/10.1063/1.468147>.
- [24] M.-C. Chan, A.R.W. McKellar, J. Chem. Phys. 105 (1996) 7910–7914, <http://dx.doi.org/10.1063/1.472707>.
- [25] N. Moazzen-Ahmadi, A.R.W. McKellar, B. Fernández, D. Farrelly, J. Chem. Phys. 142 (2015) 084312, <http://dx.doi.org/10.1063/1.4913492>.
- [26] P. Jankowski, A.R.W. McKellar, K. Szalewicz, Science 336 (2012) 1147–1150, <http://dx.doi.org/10.1126/science.1221000>.
- [27] P. Jankowski, L.A. Surin, A. Potapov, S. Schlemmer, A.R.W. McKellar, K. Szalewicz, J. Chem. Phys. 138 (2013) 084307, <http://dx.doi.org/10.1063/1.4791712>.
- [28] S. Green, Astrophys. J. Supp. Ser. 43 (1980) 103–111.
- [29] A. Palma, S. Green, D.J. Defrees, A.D. Mclean, J. Chem. Phys. 89 (1988) 1401–1407.
- [30] A. Palma, S. Green, D.J. Defrees, A.D. Mclean, Astrophys. J. Supp. Ser. 68 (1988) 287–318.
- [31] S. Green, Astrophys. J. Supp. Ser. 70 (1989) 813–831.
- [32] S. Green, D.J. Defrees, A.D. Mclean, J. Chem. Phys. 94 (1991) 1346–1359, <http://dx.doi.org/10.1063/1.459992>.
- [33] S. Maluendes, A.D. Mclean, S. Green, J. Chem. Phys. 96 (1992) 8150–8156, <http://dx.doi.org/10.1063/1.462318>.
- [34] S. Green, S. Maluendes, A.D. Mclean, Astrophys. J. Supp. Ser. 85 (1993) 181–185.
- [35] B. Kukawska-Tarnawska, G. Chalasiński, M.M. Szczesniak, J. Mol. Struct. 297 (1993) 313–325.
- [36] F.M. Tao, Z.R. Li, Y.K. Pan, Chem. Phys. Lett. 255 (1996) 179–186.
- [37] M.P. Hodges, R.J. Wheatley, A.H. Harvey, J. Chem. Phys. 116 (2002) 1397–1405, <http://dx.doi.org/10.1063/1.1421065>.
- [38] K. Patkowski, T. Korona, R. Moszynski, B. Jeziorski, K. Szalewicz, J. Mol. Struct. (Theochem.) 591 (2002) 231–243.
- [39] G. Calderoni, F. Cargnoni, M. Raimondi, Chem. Phys. Lett. 370 (2003) 233–239.
- [40] J. Makarewicz, J. Chem. Phys. 129 (2008) 184310, <http://dx.doi.org/10.1063/1.3009270>.
- [41] C.H. Yang, G. Sarma, J.J. ter Meulen, D.H. Parker, J. Phys. Chem. A 114 (2010) 9886–9892.

- [42] M. Ivanov, M.L. Dubernet, D. Babikov, J. Chem. Phys. 140 (2014) 134301, <http://dx.doi.org/10.1063/1.4868715>.
- [43] G. Tejeda, E. Carmona-Novillo, E. Moreno, J.M. Fernandez, M.I. Hernandez, S. Montero, Astrophys. J. Supp. Ser. 216 (2015) 3, <http://dx.doi.org/10.1088/0067-0049/216/1/3>.
- [44] D.-Q. Xie, H. Ran, Y. Zhou, Int. Rev. Phys. Chem. 26 (2007) 487–520, <http://dx.doi.org/10.1080/01442350701437926>.
- [45] D. Hou, Y.-T. Ma, X.-L. Zhang, H. Li, J. Chem. Phys. 144 (2016) 014301, <http://dx.doi.org/10.1063/1.4939089>.
- [46] O.L. Polyansky, P. Jensen, J. Tennyson, J. Chem. Phys. 105 (1996) 6490–6497, <http://dx.doi.org/10.1063/1.472501>.
- [47] K. Raghavachari, G.W. Trucks, J.A. Pople, M. Head-Gordon, Chem. Phys. Lett. 157 (1989) 479–483, [http://dx.doi.org/10.1016/S0009-2614\(89\)87395-6](http://dx.doi.org/10.1016/S0009-2614(89)87395-6).
- [48] D.E. Woon, T.H. Dunning Jr., J. Chem. Phys. 98 (1993) 1358–1371, <http://dx.doi.org/10.1063/1.464303>.
- [49] F.M. Tao, Y.K. Pan, Mol. Phys. 81 (1994) 507–518, <http://dx.doi.org/10.1080/00268979400100331>.
- [50] T.B. Pedersen, B. Fernandez, H. Koch, J. Makarewicz, J. Chem. Phys. 115 (2001) 8431–8439, <http://dx.doi.org/10.1063/1.1398102>.
- [51] S.F. Boys, F. Bernardi, Mol. Phys. 19 (1970) 553–556, <http://dx.doi.org/10.1080/00268977000101561>.
- [52] H.J. Werner, P.J. Knowles, R.D. Amos, A. Berning, D.L. Cooper, M.J.O. Deegan, A.J. Dobbyn, F. Eckert, S.T. Elbert, C. Hampel, R. Lindh, A.W. Lloyd, W. Meyer, A. Nicklass, K. Peterson, R. Pitzer, A.J. Stone, P.R. Taylor, M.E. Mura, P. Pulay, M. Schutz, H. Stoll, T. Thoorsteinso, MOLPRO, version 2010.1, a package of ab initio programs.
- [53] H. Wei, T. Carrington Jr., J. Chem. Phys. 97 (1992) 3029–3037, <http://dx.doi.org/10.1063/1.463044>.
- [54] J. Echave, D.C. Clary, Chem. Phys. Lett. 190 (1992) 225–230, [http://dx.doi.org/10.1016/0009-2614\(92\)85330-D](http://dx.doi.org/10.1016/0009-2614(92)85330-D).
- [55] Y.T. Ma, T. Zeng, H. Li, J. Chem. Phys. 140 (2014) 214309, <http://dx.doi.org/10.1063/1.4879956>.
- [56] T. Zeng, H. Li, R.J. Le Roy, P.-N. Roy, J. Chem. Phys. 135 (2011) 094304, <http://dx.doi.org/10.1063/1.3626840>.
- [57] D.T. Colbert, W.H. Miller, J. Chem. Phys. 96 (1992) 1982–1991, <http://dx.doi.org/10.1063/1.462100>.
- [58] L. Wang, M.H. Yang, J. Chem. Phys. 129 (2008) 174305, <http://dx.doi.org/10.1063/1.3005645>.
- [59] X.G. Wang, T. Carrington Jr., J. Chem. Phys. 134 (2011) 044313, <http://dx.doi.org/10.1063/1.3533230>.
- [60] A. van der Avoird, D.J. Nesbitt, J. Chem. Phys. 134 (2011) 044314, <http://dx.doi.org/10.1063/1.3533232>.
- [61] F.C. DeLucia, P. Helminger, R.L. Cook, W. Gordy, Phys. Rev. A 5 (1972) 487–490, <http://dx.doi.org/10.1103/PhysRevA.5.487>.
- [62] R.A. Toth, J. Mol. Spectrosc. 190 (1998) 379–396, <http://dx.doi.org/10.1006/jmsp.1998.7611>.
- [63] R.A. Toth, J. Mol. Spectrosc. 194 (1999) 28–42.
- [64] M. Wang, G. Audi, A. Wapstra, F. Kondev, M. MacCormick, X. Xu, B. Pfeiffer, Chin. Phys. C 36 (2012) 1603–2014.
- [65] J. Hutson, J. Chem. Phys. 92 (1990) 157–168, <http://dx.doi.org/10.1063/1.458485>.
- [66] X.-C. Liu, D. Hou, J. Thomas, H. Li, Y.-J. Xu, J. Mol. Spectrosc. xxx (2016) xxx.
- [67] J.-P. Lei, Y.-Z. Zhou, D.-Q. Xie, H. Zhu, J. Chem. Phys. 137 (2012) 224314, <http://dx.doi.org/10.1063/1.4770263>.
- [68] L. Wang, M.-H. Yang, J. Chem. Phys. 129 (2008) 174305, <http://dx.doi.org/10.1063/1.3005645>.
- [69] B. Fernández, C. Henriksen, D. Farrelly, Mol. Phys. 111 (2013) 1173, <http://dx.doi.org/10.1080/00268976.2013.793837>.
- [70] R.J. Le Roy, Y. Huang, C. Jary, J. Chem. Phys. 125 (2006) 164310.
- [71] R.J. Le Roy, R.D.E. Henderson, Mol. Phys. 105 (2007) 663–677, <http://dx.doi.org/10.1080/00268970701241656>.
- [72] K. Harada, K. Tanaka, T. Tanaka, S. Nanbu, M. Aoyagi, J. Chem. Phys. 117 (2002) 7041, <http://dx.doi.org/10.1063/1.1496466>.